Kinematic, Workspace and Force Analysis of a five-DOF Hybrid Manipulator R(2RPR)R/SP+RR

Yundou Xu
Yanshan University
Fan Yang
Yanshan University
Youen Mei
Yanshan University
Dongsheng Zhang
Tencent
Yulin Zhou
Yanshan University
Yongsheng Zhao (yszhao@ysu.edu.cn)
Yanshan University

Original Article

Keywords: Hybrid manipulator, Over-constrained, Kinematic analysis, Stiffness analysis

Posted Date: June 22nd, 2021

DOI: https://doi.org/10.21203/rs.3.rs-624423/v1

Kinematic, workspace and force analysis of a five-DOF hybrid manipulator R(2RPR)R/SP+RR

Yundou Xu[1,2,3], Fan Yang[1,3], Youen Mei [1,3], and Dongsheng Zhang [4], Yulin Zhou[3], Yongsheng Zhao[1,2,3*]

1. Laboratory of Parallel Robot and Mechatronic System of Hebei Province, Yanshan University, Qinhuangdao 066004, China

2. Key Laboratory of Advanced Forging & Stamping Technology and Science of Ministry of National Education, Yanshan University, Qinhuangdao 006004, China

3. School of Mechanical Engineering, Yanshan University, Qinhuangdao 066004, China

4. Tencent Robotics X, Tencent Holdings, Shenzhen 518057, China

Abstract: In the present study, the over-constrained hybrid manipulator R(2RPR)R/SP+RR is considered as the research objective. In this paper, kinematics of the hybrid manipulator, including the forward and inverse position, are analyzed. Then, the workspace is checked based on the inverse position solution to evaluate whether the workspace of the hybrid manipulator meets the requirements, and the actual workspace of the hybrid robot is analyzed. After that, the force analysis of the over-constrained parallel mechanism is carried out, and an ADAMS-ANSYS rigid-flexible hybrid body model is established to verify the simulation. Based on the obtained results from the force analysis, the manipulator structure is design. Then, the structure optimization is carried out to improve the robot stiffness. Finally, calibration and workspace verification experiments are performed on the prototype, cutting experiment of an S-shaped aluminum alloy workpiece is completed, and the experiment verifies the processing ability of the prototype and proves that the prototype has good application prospects.

Keywords: Hybrid manipulator; Over-constrained; Kinematic analysis; Stiffness analysis

1. Introduction

With the continuous acceleration of the modernization process, the complexity of specimens involved in high-end manufacturing such as parts of aircraft, automobiles and ships has increased rapidly [1]. Accordingly, requirements of positioning accuracy and machining flexibility have continuously increased in the past years.

The serial robot has large workspace and good flexibility, but it is limited in the processing field that requires high precision and rigidity of the robot body. Parallel robots have large rigidity and strong carrying capacity, but they have shortcomings such as small working space and poor flexibility. Hybrid robots, especially five-degree-of-freedom (DOF) serial-parallel hybrid robots, have the advantages of parallel and serial robots in terms of

*Corresponding author. Tel./Fax: +86-335-807-4581. E-mail address: 1657774223@qq.com, yszhao@ysu.edu.cn (Y.S. Zhao).

stiffness and workspace, respectively. Accordingly, hybrid robots have attracted many researchers and enterprises [2]–[4]. Many scholars have conducted in-depth research on the five-DOF hybrid robot. Based on the two-rotation-one-translation (2R1T) parallel mechanism [2], some processing robots with good application prospects, including Tricept hybrid robots [3], [4], Exechon hybrid processing center [5], [6], TriMule and TriVariant hybrid robots [7–10], and other robots [11–16], have been developed so far.

Zhang *et al*. [17] proposed a five-DOF hybrid mechanism R(2RPR)R/SP+RR, wherein the intersection of two revolute axes of the serial part (AC swing head) of the mechanism was located on the extension line of the SP limbs. Then, the kinematic analyses were performed in this regard. However, in the actual design of this manipulator, the intersection of two revolute axes of the serial part is located in the circumcircle center of the triangle formed by the moving platform, thereby complicating the kinematic analyses.

In order to resolve the abovementioned shortcoming, kinematics, workspace and force analyses are conducted in the present study based on a novel design. Then, the corresponding stiffness, workspace and other performance indices are analyzed. Finally, an experimental platform is constructed to evaluate the performance index and meet the expected requirements. It should be indicated that in the entire manuscript, the notations R, P, U, and S stand for revolute, prismatic, universal, and spherical joints, respectively.

2. Motion principle and kinematic analysis

2.1 Motion principle

Xu *et al*. [18], [19] present a novel design of the hybrid manipulator, and its parallel part is R(2RPR)R/SP mechanism (see Fig. 1). Each limb of the parallel part consists of upper and lower links connected to the fixed and moving platforms, respectively. Moreover, $A_1a_1(A_2a_2)$ limb form a UPU structure. Two U joints on the same side of two limbs are connected to the moving or fixed platforms and the two axes are collinear. Meanwhile, these two limbs are also recorded as a composite limb R(2RPR)R. The limb A_3a_3 is of SP structure, and the axis of P joint is perpendicular to the plane of the moving platform. Different from the mechanism described in [17], the intersection of the two revolute axes of the serial part is not located on the extension line of the SP limb.

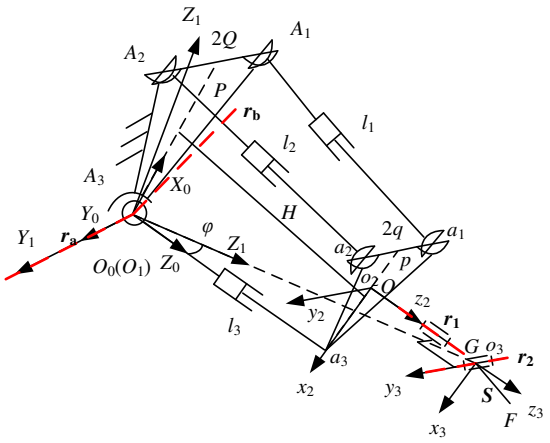

Fig. 1 Coordinate systems of the R(2RPR)R/SP+R+R hybrid manipulator.

2.2 Inverse position analysis

Fig. 1 shows the coordinate system of the hybrid robot. It indicates that the origin of the reference coordinate O_0-$X_0Y_0Z_0$ is attached to point A_3 of the fixed platform, while the X_0-axis is perpendicular to the bottom side A_1A_2 and Y_0-axis is parallel to the bottom side A_1A_2. Moreover, the origin of the coordinate system O_1-$X_1Y_1Z_1$ is at point A_3, while the corresponding Y_1-axis is parallel to the bottom side A_1A_2 and the Z_1-axis coincides with vector $\boldsymbol{A}_3\boldsymbol{G}$, where the point G is the intersection of the two revolute axes of the serial part. The origin of the coordinate system o_2-$x_2y_2z_2$ is located at the connection between the AC swing head and the moving platform with the z_2- and y_2-axes coinciding with the C swing axis $\boldsymbol{r}_1$ and the A swing axis $\boldsymbol{r}_2$, respectively. The origin of the coordinate system o_3-$x_3y_3z_3$ is located at the intersection of the AC swing head, while the corresponding z_3-axis points to the tool tip point F and the y_3-axis coincides with the A pendulum axis $\boldsymbol{r}_2$.

Given the coordinates of the proposed tool tip point $(x_F, y_F, z_F)^{\mathrm{T}}$ and the unit vector of the spindle head $\boldsymbol{S}$, the inverse position analysis is carried out to calculate the lengths l_1, l_2 and l_3 of the parallel mechanism and the angles ψ_1 and ψ_2 of the AC swing head. Then the coordinate of a_i in the O_1-$X_1Y_1Z_1$ coordinate system can be obtained as the following:

$$\begin{cases} \boldsymbol{a}_1^1 = [\,pc\varphi - l_3 s\varphi \quad -q \quad l_3 c\varphi + ps\varphi\,] \\ \boldsymbol{a}_2^1 = [\,pc\varphi - l_3 s\varphi \quad q \quad l_3 c\varphi + ps\varphi\,] \\ \boldsymbol{a}_3^1 = [\,-l_3 s\varphi \quad 0 \quad l_3 c\varphi\,] \end{cases} \tag{1}$$

Moreover, φ is the angle between Z_1-axis and vector $\boldsymbol{A}_3\boldsymbol{a}_3$. It should be indicated that in all calculations, the length of the bottom side of the moving platform triangle is $2q$ and the height is p. Based on (1), φ can be expressed in the form below:

$$\varphi = \arcsin\left(\frac{p}{2L_G}\right) \tag{2}$$

where $L_G = \sqrt{x_G^2 + y_G^2 + z_G^2}$ is the length from the point G to O_0, then

$$l_3 = \sqrt{L_G^2 - \left(\frac{p}{2}\right)^2} - k \tag{3}$$

where k is the distance between the intersection point G of the AC head axes and the point O. The coordinate of the intersection point G can be derived as follows:

$$\begin{cases} \boldsymbol{G}_x = \boldsymbol{x}_F - \boldsymbol{f}[1 \quad 0 \quad 0]\boldsymbol{S} \\ \boldsymbol{G}_y = \boldsymbol{y}_F - \boldsymbol{f}[0 \quad 1 \quad 0]\boldsymbol{S} \\ \boldsymbol{G}_z = \boldsymbol{z}_F - \boldsymbol{f}[0 \quad 0 \quad 1]\boldsymbol{S} \end{cases} \tag{4}$$

where, f is the distance from the tool tip to the point G, the orientation of the moving system O_1-$X_1Y_1Z_1$ relative to the reference coordinate system O_0-$X_0Y_0Z_0$ can be represented by a rotation matrix described by Euler angles (α, β, γ). This can be mathematically expressed in the form below:

$${}^0_1\boldsymbol{R} = \begin{bmatrix} \boldsymbol{c}\beta\boldsymbol{c}\gamma & -\boldsymbol{c}\beta\boldsymbol{s}\gamma & \boldsymbol{s}\beta \\ \boldsymbol{c}\alpha\boldsymbol{s}\gamma + \boldsymbol{c}\gamma\boldsymbol{s}\alpha\boldsymbol{s}\beta & \boldsymbol{c}\alpha\boldsymbol{c}\gamma - \boldsymbol{s}\alpha\boldsymbol{s}\beta\boldsymbol{s}\gamma & -\boldsymbol{c}\beta\boldsymbol{s}\alpha \\ \boldsymbol{s}\alpha\boldsymbol{s}\gamma - \boldsymbol{c}\alpha\boldsymbol{c}\gamma\boldsymbol{s}\beta & \boldsymbol{c}\gamma\boldsymbol{s}\alpha + \boldsymbol{c}\alpha\boldsymbol{s}\beta\boldsymbol{s}\gamma & \boldsymbol{c}\alpha\boldsymbol{c}\beta \end{bmatrix} \tag{5}$$

where $s\alpha$ and $c\alpha$ denote $\sin\alpha$ and $\cos\alpha$, respectively. Moreover, the coordinate of point G can be expressed as:

$$\begin{bmatrix} x_G \\ y_G \\ z_G \end{bmatrix} = {}^0_1\boldsymbol{R} \begin{bmatrix} 0 \\ 0 \\ L_G \end{bmatrix} \tag{6}$$

Then,

$$\begin{cases} \alpha = \arctan\left(-\dfrac{y_G}{z_G}\right) \\ \beta = \arcsin\left(\dfrac{x_G}{L_G}\right) \end{cases} \tag{7}$$

According to the structural constraints of the mechanism, four points A_1, A_2, a_1, and a_2 are always in the same plane. Then the coupling angle γ can be calculated from the following expression:

when $y_G = 0$,

$$\gamma = \arcsin\left(\frac{w}{\sqrt{u^2 + v^2}}\right) - \arctan 2\left(\frac{v}{\sqrt{u^2 + v^2}}, \frac{u}{\sqrt{u^2 + v^2}}\right) \tag{8}$$

when $y_G \neq 0$,

$$\gamma = 2\arctan\left(\frac{u+\sqrt{u^2+v^2-w^2}}{v+w}\right) \tag{9}$$

$$\begin{cases} u = Pqc\alpha s\beta - q\left(L_G c\varphi + ps\varphi\right)c\alpha \\ v = Pqs\alpha - q\left(L_G c\varphi + ps\varphi\right)c\alpha s\beta \\ w = q\left(pc\varphi - L_G s\varphi\right)s\alpha c\beta \end{cases} \tag{10}$$

where P denotes the fixed platform triangle height. Subsequently, the length of the three branches of the parallel mechanism can be obtained from the following expression:

$$l_i = \left\| {}^0_1\boldsymbol{R}\boldsymbol{a}_i^1 - \boldsymbol{A}_i \right\| (i = 1,2,3) \tag{11}$$

The rotation matrix of the coordinate system o_3-$x_3y_3z_3$ relative to the fixed coordinate system can be expressed as:

$$\boldsymbol{R} = {}^0_1\boldsymbol{R}\boldsymbol{R}_{\varphi}\,{}^1_2\boldsymbol{R}\,{}^2_3\boldsymbol{R} \tag{12}$$

where $\boldsymbol{R}_{\varphi}$ is the rotation matrix respect to φ. Moreover, ${}^1_2\boldsymbol{R}$ and ${}^2_3\boldsymbol{R}$ denote the rotation matrices of the two rotation axes of the AC swing head, they can be obtained from the following expression

$$\boldsymbol{R}_{\varphi} = \begin{bmatrix} -c\varphi & 0 & s(-\varphi) \\ 0 & 1 & 0 \\ -s(-\varphi) & 0 & c(-\varphi) \end{bmatrix}, {}^1_2\boldsymbol{R} = \begin{bmatrix} c\psi_1 & -s\psi_1 & 0 \\ s\psi_1 & c\psi_1 & 0 \\ 0 & 0 & 1 \end{bmatrix}, \text{and } {}^2_3\boldsymbol{R} = \begin{bmatrix} c\psi_2 & 0 & s\psi_2 \\ 0 & 1 & 0 \\ -s\psi_2 & 0 & c\psi_2 \end{bmatrix}.$$

The unit vector of the spindle head can be expressed as:

$${}^0_1\boldsymbol{R}\boldsymbol{R}_{\varphi}\,{}^1_2\boldsymbol{R}\,{}^2_3\boldsymbol{R}\begin{bmatrix} 0 \\ 0 \\ 1 \end{bmatrix} = \boldsymbol{S} \tag{13}$$

The two input angles of the AC swing head can be solved as the following:

$$\begin{cases} \psi_1 = \arctan\left(\dfrac{\begin{bmatrix} 0 & 1 & 0 \end{bmatrix}\boldsymbol{R}_{\varphi}^{\boldsymbol{T}}\,{}^0_1\boldsymbol{R}^{\boldsymbol{T}}\boldsymbol{S}}{\begin{bmatrix} 1 & 0 & 0 \end{bmatrix}\boldsymbol{R}_{\varphi}^{\boldsymbol{T}}\,{}^0_1\boldsymbol{R}^{\boldsymbol{T}}\boldsymbol{S}}\right) \\ \psi_2 = \arccos\left(\begin{bmatrix} 0 & 0 & 1 \end{bmatrix}\boldsymbol{R}_{\varphi}^{\boldsymbol{T}}\,{}^0_1\boldsymbol{R}^{\boldsymbol{T}}\boldsymbol{S}\right) \end{cases} \tag{14}$$

Since the lengths l_1, l_2 and l_3 of the parallel part and the angles ψ_1 and ψ_2 of the AC swing head can be calculated from the foregoing expressions, the inverse position analysis of the robot is completed. It is worth noting that these parameters can be used for trajectory planning and workspace calculation.

2.2 Forward position analysis

In the forward position analysis, the lengths of three limbs of the parallel part (i.e. l_1, l_2 and l_3) and the two

input angles of the AC swing head (i.e. ψ_1 and ψ_2) are known values. Accordingly, the main purpose of this analysis is to solve the coordinate of the tool tip point F and the unit vector of the spindle head $\boldsymbol{S}$.

The orientation of the moving platform coordinate system O_1-$X_1Y_1Z_1$ relative to the fixed platform coordinate system O_0-$X_0Y_0Z_0$ can be described by the rotation matrix ${}_1^0\boldsymbol{R}$. The position of point a_i on the moving platform in the coordinate system O_0-$X_0Y_0Z_0$ can be expressed in the form below:

$$\begin{cases} \boldsymbol{a}_1^0 = {}_1^0\boldsymbol{R}\boldsymbol{a}_1^1 \\ \boldsymbol{a}_2^0 = {}_1^0\boldsymbol{R}\boldsymbol{a}_2^1 \\ \boldsymbol{a}_3^0 = {}_1^0\boldsymbol{R}\boldsymbol{a}_3^1 \end{cases} \tag{15}$$

The expression $l_i = \left\| \boldsymbol{a}_i^0 - \boldsymbol{A}_i \right\|$ (i=1, 2, 3) is a system of ternary higher order equations. In the present study, 'Fsolve' function of MATLAB software was applied to calculate three rotation angles α, β, γ in ${}_1^0\boldsymbol{R}$. The position of the point G in the coordinate system O_1-$X_1Y_1Z_1$ of the moving platform can be expressed as follows:

$${}^1\boldsymbol{G} = \begin{pmatrix} 0 & 0 & l_4 \end{pmatrix}^{\mathrm{T}} \tag{16}$$

where l_4 is the length from point A_3 to point G and $l_4 = \sqrt{(l_3 + k)^2 + \dfrac{p^2}{4}}$.

Meanwhile, the position of the point G in the fixed platform coordinate system O_0-$X_0Y_0Z_0$ can be obtained as the following:

$$\boldsymbol{G} = {}_1^0\boldsymbol{R}\,{}^1\boldsymbol{G} = \begin{pmatrix} x_G & y_G & z_G \end{pmatrix}^{\mathrm{T}} \tag{17}$$

The rotation matrix $\boldsymbol{R}$ of the end coordinate system of the mechanism can be expressed as:

$$\boldsymbol{R} = {}_1^0\boldsymbol{R}\boldsymbol{R}_{\varphi}\,{}_2^1\boldsymbol{R}\,{}_3^2\boldsymbol{R} \tag{18}$$

Based on the foregoing expressions, the unit vector of the spindle head $\boldsymbol{S}$ can be derived in the form below:

$$\boldsymbol{S} = {}_1^0\boldsymbol{R}\boldsymbol{R}_{\varphi}\,{}_2^1\boldsymbol{R}\,{}_3^2\boldsymbol{R}\begin{bmatrix} 0 \\ 0 \\ 1 \end{bmatrix} \tag{19}$$

Moreover, the coordinates of the tool tip point F are obtained as:

$$\begin{cases} \boldsymbol{x}_F = \boldsymbol{x}_G + \boldsymbol{f}(1 \quad 0 \quad 0)\boldsymbol{S} \\ \boldsymbol{y}_F = \boldsymbol{y}_G + \boldsymbol{f}(0 \quad 1 \quad 0)\boldsymbol{S} \\ \boldsymbol{z}_F = \boldsymbol{z}_G + \boldsymbol{f}(0 \quad 0 \quad 1)\boldsymbol{S} \end{cases} \tag{20}$$

The coordinate vector $\boldsymbol{F} = (x_F \quad y_F \quad z_F)^{\mathrm{T}}$ of the tool tip point and the unit vector of the spindle head $\boldsymbol{S}$ can be obtained, which can be used for real-time detection of the machining process.

3. Workspace analysis

3.1 Workspace check

According to the performed manipulator kinematics analysis, the workspace of the manipulator can be searched based on the inverse position analysis. However, it is necessary to check whether the workspace represented by the intersection of the two rotation axes of the AC swing head meets the size of a ϕ1300 mm× 300 mm cylinder.

In this regard, a large enough space containing the expected workspace [15] is considered at the first step. Then the points in the predetermined three-dimensional space are transformed into the inverse position solution of the mechanism, and the driving values of the mechanism are obtained to determine whether it is inside or outside the workspace. In the former case, the transformed point is printed, while in the latter case, the next point is selected to judge until all points in the space are searched. Finally, all points that meet the mechanism constraints are imported into the computational domain to form a three-dimensional appearance of the workspace, as shown in Fig. 2.

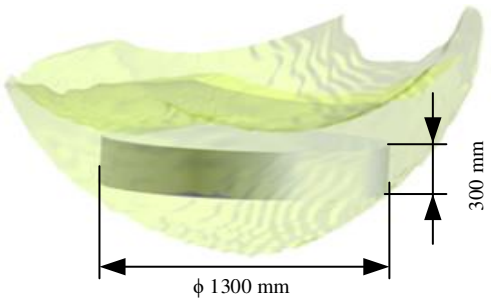

Fig. 2 Workspace appearance.

Fig. 2 indicates that the size of the manipulator's workspace can cover a ϕ1300 mm × 300 mm cylinder, which meets the requirements of the expected workspace.

3.2 Actual workspace

In the practical working condition, the center of the end face of the AC swing head where the tool holder is installed is normally, *F*, i.e., the tool tip point, considered as the workspace reference point. It should be indicated that there are certain requirements for the angle ranges of the A- and C-axes of the AC swing head. The angle ranges of the A- and C-axes at the AC swing head are set to ±40°, the actual effective stroke of each limb is 800 mm. Since the solution of the actual workspace is similar to the presented analysis based on the inverse kinematics solution, the actual workspace can be solved by increasing the constraints of angle limits of the AC swing head.

Fig. 3 shows the actual workspace of the five-DOF hybrid manipulator in the MATLAB environment. The height of the actual workspace is 800 mm, the overall shape is similar to a mushroom, the head is convex, the

bottom is concave, the middle part is relatively sharp and thick, and the surrounding boundary is blunt and thin.

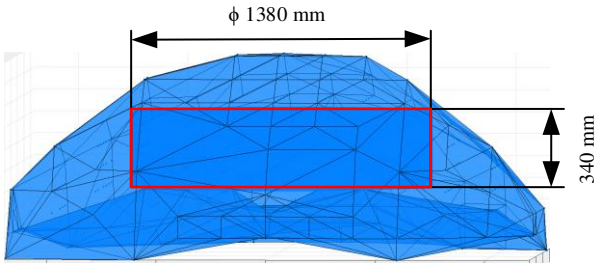

Fig. 3 Appearance of the real workspace.

It is worth noting that considering the small size of the head and bottom, an effective workspace cannot be formed. As a result, the workspace is concentrated in the middle. Meanwhile, the actual workspace is much larger than the planning workspace, which can meet the processing requirements.

In the present study, a ϕ1380 mm × 340 mm cylinder is considered as the actual workspace. It is observed that the size of the manipulator's actual workspace is larger than the positional workspace. It can completely include a ϕ1380 mm×340 mm cylinder, which exceeds the requirement workspace.

4. Force analysis and structural optimization design

4.1 Force analysis and simulation verification

In order to provide a theoretical basis for the structural design of the hybrid manipulator, force analysis should be carried out. On the other hand, the parallel mechanism of the manipulator R(2RPR)R/SP contains over-constraints, which generate static indeterminate problems in the force analysis. In order to resolve this problem, the weighted generalized inverse method [20], [21] is applied in the present study. Then the analytical solution of the force analysis of the over-constrained parallel mechanisms can be expressed as follows:

$$\boldsymbol{f} = \boldsymbol{W}^{-1}(\boldsymbol{G}_f^F)^{\mathrm{T}}\left(\boldsymbol{G}_f^F\boldsymbol{W}^{-1}(\boldsymbol{G}_f^F)^{\mathrm{T}}\right)^{-1}\$_F \tag{21}$$

where $\boldsymbol{G}_f^F = \left(\$_{a1} \quad \$_1^r \quad \$_{a2} \quad \$_2^r \quad \$_{a3} \quad \$_{31}^r \quad \$_{32}^r\right)$ is the mapping matrix from $\boldsymbol{f}$ to $\$_F$, $\$_F$ denotes external forces exerted to the moving platform and $\boldsymbol{f} = \left(f_{a,1} \quad m_{r,1} \quad f_{a,2} \quad m_{r,2} \quad f_{a,3} \quad f_{r,31} \quad f_{r,32}\right)$ is the column vector composed of the magnitudes of the constraint and actuation wrenches. Moreover, $\boldsymbol{W}$ is the weighting matrix, composed of the stiffness of the constrained wrenches, which can be determined by the stiffness of each limb structure.

In the present study, it is assumed that limbs are cylindrical rods of equal cross-section, and the structural parameters are given as follows:

Table I The structural parameters.

Parameters	value
E	2.07×1011 Pa
μ	0.29
H	0.335 m
$2Q$	0.3 m
$2q$	0.18 m
θ_1	[-π/6~π/6]
θ_2	[-π/9~π/9]
$\$_F$	(10 N 10 N 10 N; 10 N·m 10 N·m 10 N·m)

In Table 1, E represents the elastic modulus, μ represents the Poisson's ratio, H represents the initial distance between the moving and fixed platforms, and $2Q$ and $2q$ represent the base length of the fixed and moving platforms triangle, respectively. The angles that the parallel mechanism rotates around the two rotational axes $\boldsymbol{r}_a$ and $\boldsymbol{r}_b$ [17] are θ_1 and θ_2, respectively. In the moving coordinate system o-xyz, the external load $\$_F$ is applied at the origin of the moving platform. Then constraint forces/couples and driving forces of each limb can be solved. Figs. 4-6 present obtained results in this regard.

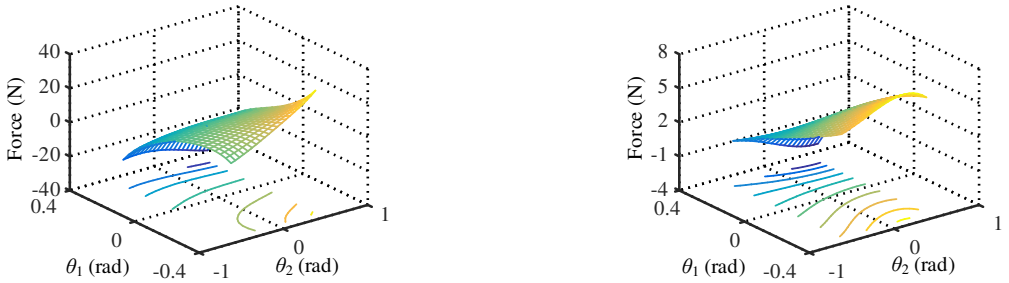

(a) Driving force (b) Constraint force

Fig. 4 Constraint wrenches distribution of the limb $U_{11}P_1U_{12}$

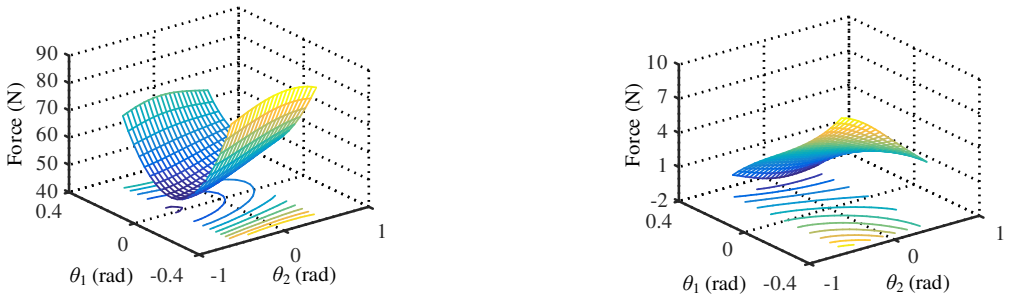

(a) Driving force (b) Constraint force

Fig. 5 Constraint wrenches distribution of the limb $U_{21}P_2U_{22}$

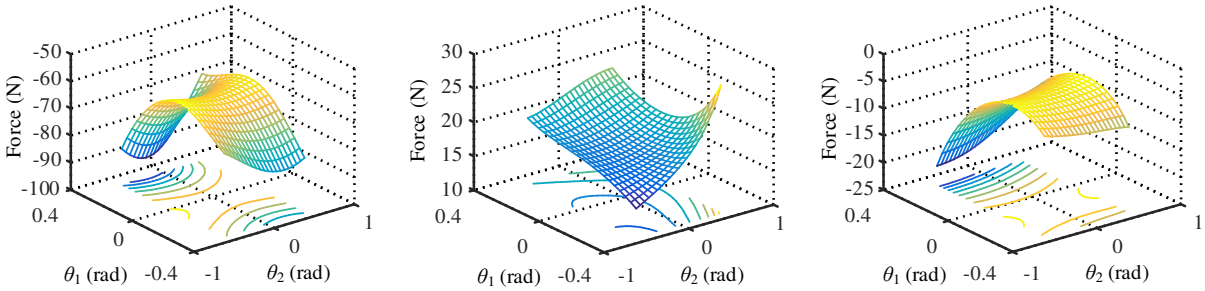

(a) Driving force (b) Constraint force 1 (c) Constraint force 2

177 Fig. 6 Constraint wrenches distribution of the limb S_3P_3.

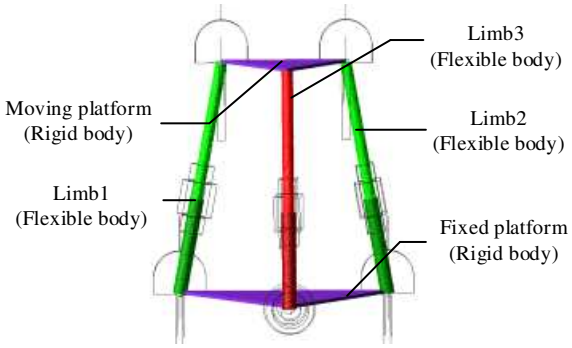

178

179 Fig. 7. Simulation model of the ADAMS-ANSYS rigid-flexible hybrid body.

180 To evaluate the accuracy of the performed force analysis, the simulation model of the ADAMS-ANSYS
181 rigid-flexible hybrid body is established, as shown in Fig. 7. It is observed that in the coordinate system o_2-
182 $x_2y_2z_2$, the above $\$_F$ is applied at the moving platform. For t = 0~1s, the moving platform has a trajectory
183 $P(z) = 0.335 + 0.005t(m)$ along the z_2-direction. Moreover, the magnitude of each limb's driving force and
184 constraint forces/couples can be measured in the simulation model, and the results are shown in Fig. 8.

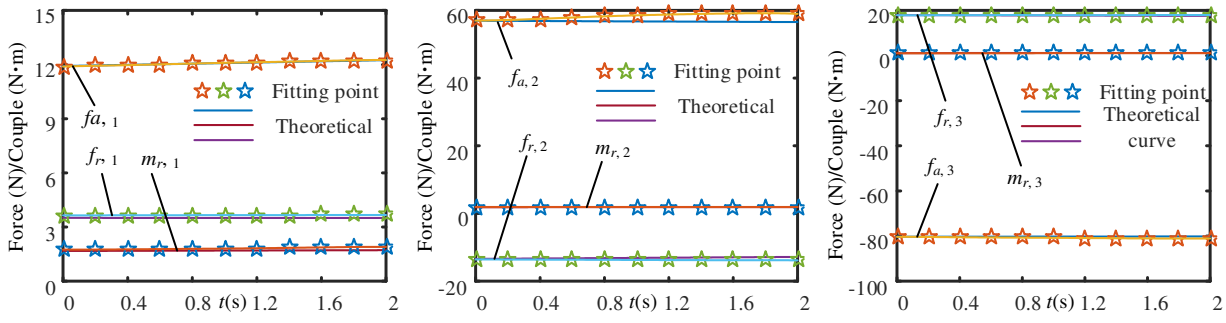

(a) $U_{11}P_1U_{12}$ limb1 (b) $U_{21}P_2U_{22}$ limb2 (c) S_3P_3 limb3

185 Fig. 8. Curves of the magnitude of constraint (driving) forces/couples.

186 When the mechanism is in the initial position (i.e. t = 0 and $\alpha = \beta = 0^{\circ}$), the theoretical values of the
187 magnitude of each limb's driving force, constraint forces/couples and the simulation ones are shown in Table 2.

Table II Theoretical and simulation values.

Limb	D_f/C_f	T_v	S_v	A_e	R_e
Limb1	$f_{a,1}$	4.0561 N	3.981 N	0.0751	1.85%
	$m_{r,1}$	3.0784 N·m	3.182 N·m	-0.1036	-3.37%
Limb2	$f_{a,2}$	49.094 8N	48.08 N	1.0148	2.07%
	$m_{r,2}$	3.0784 N·m	3.186 N·m	-0.1076	-3.50%
Limb3	$f_{a,3}$	-62.8534 N	-62.66 N	-0.1934	0.31%
	$f_{r,31}$	17.9403 N	18.35 N	-0.4097	-2.28%
	$f_{r,32}$	-5.7550 N	-5.87 N	0.115	-2.00%

In Table 2, the D_f/C_f represents driving/constraint force, the T_v/S_v represents theoretical/simulation value, the A_e/R_e represents absolute/relative error. From Table 2, we know that the error between the theoretical and the simulation data is negligible, which proves the accuracy of the obtained results from the simulation and theoretical analysis. It is concluded that the performed analysis can be applied as the basis for subsequent manipulator design.

4.2 Structural design based on the stiffness optimization

Based on the force analysis and simulation results, the structure design of the five-DOF hybrid manipulator was completed. In the actual mechanism design process, specific structural forms and arrangements of components should be considered. In order to improve the stiffness of the manipulator and ensure the stiffness consistency along the lateral direction, the structure should be optimized. The stiffness performance results of the manipulator are obtained through finite element analysis. In this regard, Fig. 9 presents the deformation contour.

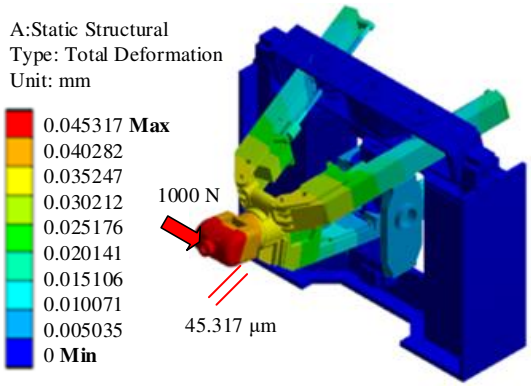

Fig. 9. Deformation of the manipulator originating from the applied load along the X-direction.

Accordingly, as shown in Fig.9, under the external load, the maximum deformation of each component of the hybrid manipulator can be obtained, and the weak area of the 3D model can be obtained. the manipulator structure has been optimized and analyzed considering the principle of lightweight to improve the rigidity of the manipulator. Through multiple rounds of iteration and calculation analysis, the optimization process is omitted, and the finite element analysis results of international products Exechon as the goal, the optimized 3D model of the hybrid manipulator is obtained in Fig. 10. And Fig. 11 reveals that under the same loading condition as that in Fig. 9, the maximum deformation of the end-effector of the optimized hybrid manipulator is 0.033891 mm and the calculated lateral stiffness increases from 22 N/μm to 29.5 N/μm, indicating that the hybrid manipulator has high stiffness and a good application prospect.

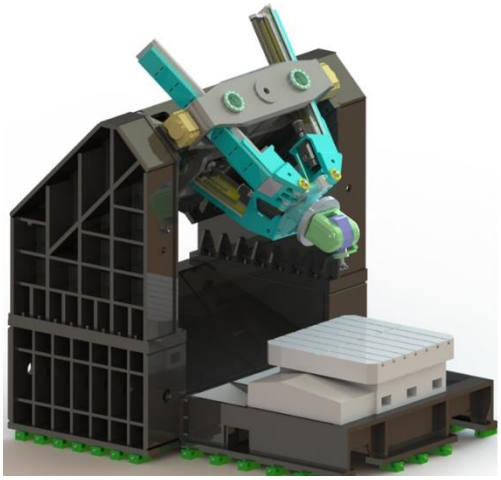

Fig. 10. 3D model of the optimized hybrid manipulator.

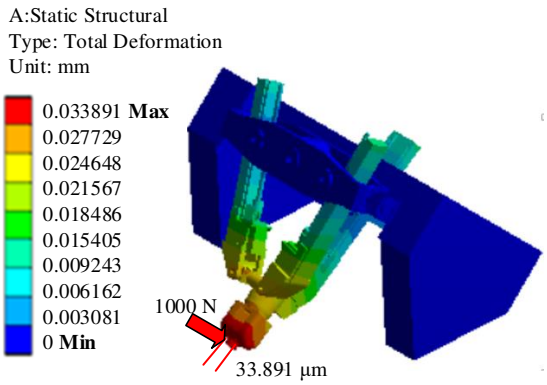

Fig. 11. Deformation of the optimized manipulator originating from the applied load along the X-direction.

5 Prototype and experiments

The prototype was manufactured based on the optimized 3D model, and the designed manipulator was calibrated by the laser tracker system. After compensation based on calibration data, experimental results show that the average positioning accuracy along the *X*-, *Y*-, and *Z*-directions are 0.0445, 0.0404, and 0.0164 mm,

respectively [22-23].

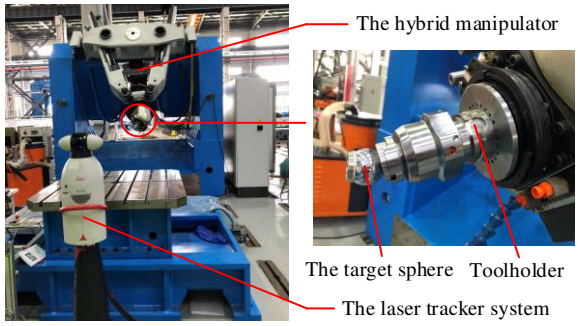

Fig. 12. The prototype of the 5-DOF hybrid manipulator.

Then the re-position accuracy in four configurations, called B_1, B_2, B_3, and B_4 configurations, are measured and the results are presented in Table 3. Finally, the size of the workspace to reach the calculated size is verified. Let the end of the manipulator take a motion trajectory of a ϕ1300 mm circle and run it several times in space. The coordinates of the endpoints are captured by a laser tracker system. The distance between the nearest and the farthest trajectory is 330 mm. Moreover, when the manipulator moves to any point on the given trajectory, the length of each branch meets the design requirements and no alarms appeared on the branch limit switches. Consequently, it is concluded that the workspace meets the requirements.

Table III The re-position accuracy with different configurations.

Re-position accuracy (mm)			
B_1	B_2	B_3	B_4
0.0164	0.0420	0.0461	0.0256

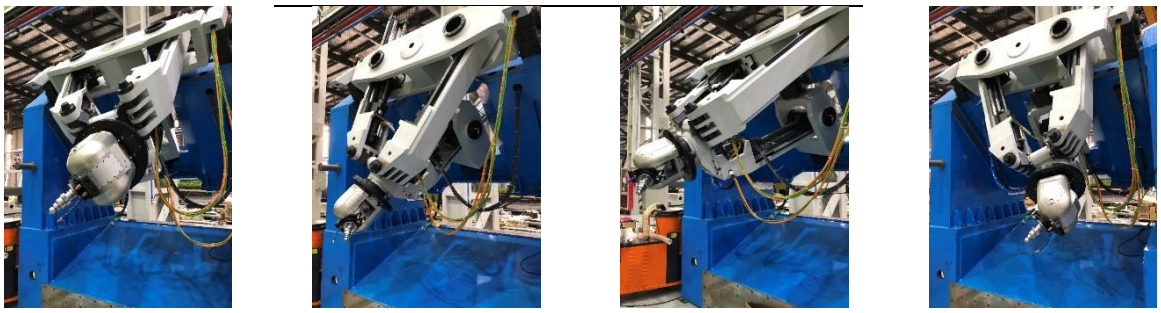

(a) Configuration B_1 (b) Configuration B_2 (c) Configuration B_3 (d) Configuration B_4

Fig. 13. Four configurations for measuring the re-position accuracy.

Finally, a cutting experiment of an S-shaped aluminum alloy workpiece is planned to verify the machining ability of the hybrid manipulator prototype.

(a) Cutting process moment

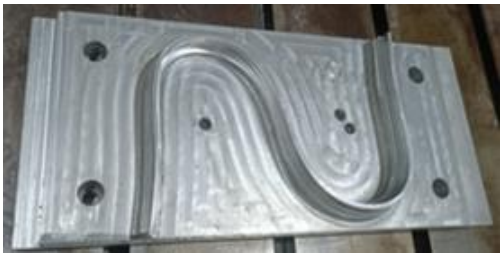

(b) workpiece

Fig. 14. The cutting process moment and the workpiece.

Fig. 14 (a) shows the cutting process moment of machining aluminum alloy components by the hybrid manipulator prototype. Fig. 14 (b) shows the S-shaped aluminum alloy workpiece processed by the prototype. The S-shaped workpiece exhibits a certain spatial surface with a good machining surface quality. It is concluded that the designed hybrid robot has good machining capabilities.

Conclusions

(1) In the present study, the intersection of the two rotation axes of the AC swing head is considered in the triangle formed by the moving platform, and the forward and inverse position of the five-DOF hybrid manipulator are solved for the hybrid mechanism R(2RPR)R/SP+RR. In particular, the analytical solution of the inverse position is derived. The presented solution is expected to become an important foundation for the subsequent motion control, parameter calibration and compensation. Then the robot's actual workspace that calculated with the tool tip point as the reference point is analyzed based on the kinematic calculation results, the calculation results show that it can meet the requirement workspace.

(2) Force analysis of the overconstrained parallel mechanism R(2RPR)R/SP is conducted by the weighted generalized inverse method, and an ADAMS-ANSYS rigid-flexible hybrid body model is applied to verify the simulation. Based on the finite element analysis results, the structure optimization design of the hybrid manipulator is completed and the manipulator stiffness is effectively improved.

(3) It is found that after the calibration, the positioning and re-position accuracies greatly improve and meet the expected requirements. Meanwhile, the workspace of the endpoint of the prototype meets the expected requirements. The S-shaped workpiece machining concluded the designed hybrid robot has good machining capabilities.

Declarations:

Availability of data and materials

The datasets used and/or analysed during the current study are available from the corresponding author on

reasonable request.

Competing interests

The authors declare that they have no competing interests.

Funding

This work was supported by the National Natural Science Foundation of China under Grant 51875495, the National Key R&D Program of China under Grant 2017YFB1301901, and Hebei Science and Technology Project under Grant 206Z1805G.

Authors' contributions

Yongsheng zhao was responsible for the planning of the content and writing, Yundou Xu analyzed the principle of design and force analysis, Fan Yang and Youen Mei performed the kinematic, workspace analysis, experimental analyses, Dongsheng Zhang and Yulin zhou were major contributors in writing the manuscript. All authors read and approved the final manuscript.

Acknowledgements

Not applicable.

References

[1] Z. X. Zhou, T. Y. Zhou, and Y. H. Ren, “Current Research and Development Trends of Complex Surface Machining Technology,” Journal of Mechanical Engineering, vol. 46, no. 17, pp. 105-113, 2010.

[2] Q. C. Li, X. X. Chai, and Q. H. Chen, “Review on 2R1T 3-DOF parallel mechanisms,” Chinese Science Bulletin, vol. 62, no. 14, pp. 1507-1519, 2017.

[3] F. Caccavale, B. Siciliano, and L. Villani, “The Tricept robot: dynamics and impedance control,” Mechatronics IEEE/ASME Transactions on, vol. 8, no. 2, pp. 263-268, 2003.

[4] J. L. Olazagoitia and S. Wyatt, “New PKM Tricept T9000 and Its Application to Flexible Manufacturing at Aerospace Industry,” Sae Technical Papers, vol. 2007, no. 2142, pp. 37-48, 2007.

[5] Y. Zhao, Y. Jin, and J. Zhang, “Kinetostatic modeling and analysis of an exechon parallel kinematic machine (PKM) module,” Chinese Journal of Mechanical Engineering, vol. 29, no. 1, pp. 33-44, 2016.

[6] Y. Jin, Z. M. Bi, H. T. Liu, C. Higgins, M. Price, W. H. Chen, and T. Huang, “Kinematic Analysis and Dimensional Synthesis of Exechon Parallel Kinematic Machine for Large Volume Machining,” Journal of Mechanisms & Robotics, vol. 7, no. 4, pp. 41004, 2015.

[7] T. Huang, C. Dong, H. Liu, T. Sun, and D.G. Chetwynd, “A simple and visually orientated approach for type synthesis of overconstrained 1T2R parallel mechanisms,” Robotica, vol. 37, no. 7, pp. 1161-1173,

2019.

[8] T. Huang, C. Dong, H. Liu, X. Qin, J. Mei, Q. Liu, and M. Wang, “FIVE-DEGREE-OF-FREEDOM HYBRID ROBOT WITH ROTATIONAL SUPPORTS,” US, Patent 9943967, Apr. 27, 2017.

[9] M. Li, T. Huang, D. G. Chetwynd, and S. J. Hu, “Forward Position Analysis of the 3-DOF Module of the TriVariant: A 5-DOF Reconfigurable Hybrid Robot,” Journal of Mechanical Design, vol. 128, no. 1, pp. 319-322, 2005.

[10] Y.Y. Wang, T. Huang, X.M. Zhao, J.P. Mei, and S.J. Hu, “Finite Element Analysis and Comparison of Two Hybrid Robots-the Tricept and the TriVariant”, in Proc. Intelligent Robots and Systems, 2006 IEEE/RSJ International Conference on, 2006.

[11] X. J. Liu, L. P. Wang, F. Xie, and I. A. Bonev, “Design of a Three-Axis Articulated Tool Head With Parallel Kinematics Achieving Desired Motion/Force Transmission Characteristics,” Journal of Manufacturing Science & Engineering, vol. 132, no. 2, pp. 237-247, 2010.

[12] F. Xie, X. J. Liu, and J. Wang, “A 3DOF parallel manufacturing module and its kinematic optimization,” Robotics and Computer-Integrated Manufacturing, vol. 28, no. 3, pp. 334-343, 2012.

[13] Q. Li and J.M. Herve, “Type Synthesis of 3-DOF RPR-Equivalent Parallel Mechanisms,” IEEE T. Robot., vol. 30, no. 6, pp. 1333-1343, 2014, doi: 10.1109/TRO.2014.2344450.

[14] D. S. Zhang, Y. D. Xu, J. T. Yao, and Y. S. Zhao, “Analysis and Optimization of a Spatial Parallel Mechanism for a New 5-DOF Hybrid Serial-Parallel Manipulator,” Chinese Journal of Mechanical Engineering, vol. 31, no. 1, pp. 1-9, 2018.

[15] Y. Xu, D. Zhang, J. Yao, and Y. Zhao, “Type synthesis of the 2R1T parallel mechanism with two continuous rotational axes and study on the principle of its motion decoupling,” Mechanism and Machine Theory, vol. 108, pp. 27-40, 2017.

[16] Y. Xu, F. Yang, Z. Xu, J. Yao, and Y. Zhao, “TriRhino: a five-DOF hybrid serial-parallel manipulator with all rotating axes being continuous: stiffness analysis and experiments,” Journal of Mechanisms and Robotics, vol. 13, no. 2, pp. 1-15, 2020.

[17] D. Zhang, Y. Xu, J. Yao, and Y. Zhao, “Design of a novel 5-DOF hybrid serial-parallel manipulator and theoretical analysis of its parallel part,” Robotics and Computer-Integrated Manufacturing, vol. 53, pp. 228-239, 2018, doi: 10.1016/j.rcim.2018.04.004.

[18] Y. Xu, Z. Xu, F. Yang, Y. Mei, and Y. Zhao, Springer, Singapore. Design and Analysis of a New 5-DOF Hybrid Serial-Parallel Manipulator. Presented at Recent Advances in Mechanisms, Transmissions and

Applications. MeTrApp 2019. [Online]. Available: https://doi.org/10.1007/978-981-15-0142-5_30

[19] Y. Xu, Z. Xu, F. Yang, Y. Zhao, Y. Mei, Y. Zhou, J. Yao, and Y. Zhao, “Design and Analysis of a New 5-DOF Hybrid Robot Considering Workspace and Force Transmission Efficiency.” China Mechanical Engineering, vol. 30, no. 16, pp. 1996-2002, 2019.

[20] W. Liu, Y. Xu, J. Yao, and Y. Zhao, “The weighted Moore–Penrose generalized inverse and the force analysis of overconstrained parallel mechanisms,” Multibody Syst. Dyn., pp. 1-21, 2016.

[21] Y. Xu, W. Liu, J. Yao, and Y. Zhao, “A method for force analysis of the overconstrained lower mobility parallel mechanism,” Mechanism and Machine Theory, vol. 88, pp. 31-48, 2015.

[22] H. Ye, D. Wang, J. Wu, Y. Yue, and Y. Zhou, “Forward and inverse kinematics of a 5-DOF hybrid robot for composite material machining,” Robotics and Computer-Integrated Manufacturing, vol. 65, pp. 101961, 2020.

[23] Long Huang, Lairong Yin, Bei Liu, Yang Yang, Design and Error Evaluation of Planar 2-DOF Remote Center of Motion Mechanisms with Cable Transmissions. Journal of Mechanical Design, 2021，143(1), 013301-1-12. https://doi.org/10.1115/1.4047519.